Copyright WILEY-VCH Verlag GmbH & Co. KGaA, 69469 Weinheim, Germany, 2020.

Supporting Information

for *Small*, DOI: 10.1002/smll.201906768

Layer-by-Layer Assembled Oxide Nanoparticle Electrodes with High Transparency, Electrical Conductivity, and Electrochemical Activity by Reducing Organic Linker-Induced Oxygen Vacancies

Ikjun Cho, Yongkwon Song, Sanghyuk Cheong, Younghoon Kim, and Jinhan Cho**

Supporting Information

Layer-by-Layer Assembled Oxide Nanoparticle Electrodes with High Transparency, Electrical Conductivity, and Electrochemical Activity by Reducing Organic Linker-Induced Oxygen Vacancies

Ikjun Cho,[§] *Yongkwon Song,*[§] *Sanghyuk Cheong, Younghoon Kim,* and Jinhan Cho**

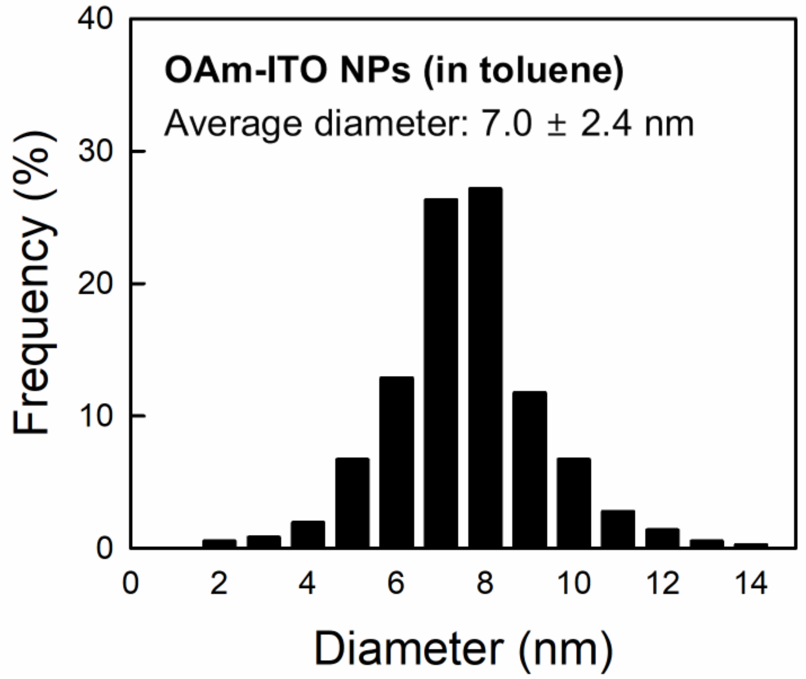

Figure S1. Size distribution histogram of OAm-ITO NPs measured from HR-TEM images.

Table S1. Element analysis of OAm-ITO NPs. Concentration and percentage of indium (In) and tin (Sn) within the prepared OAm-ITO NPs that were measured by inductively coupled plasma atomic emission spectroscopy (ICP-AES).

Elements	**Indium (In)**	**Tin (Sn)**
Concentration (ppm)	6.57×10^5	6.62×10^4
Percentage of elements [Element/(In + Sn)] (%)	90.8%	9.2%

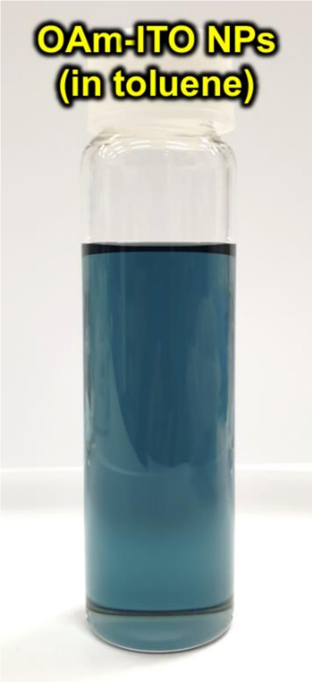
OAm-ITO NPs
(in toluene)

Figure S2. Photographic image of OAm-ITO NPs with high dispersion stability in toluene.

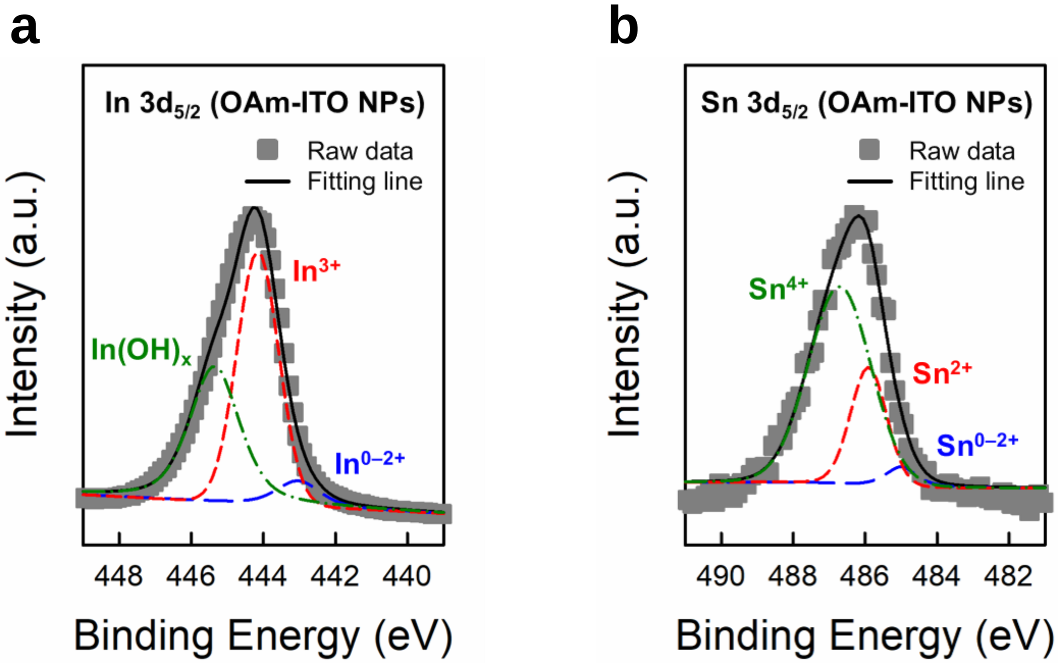

Figure S3. Deconvoluted XPS spectra of a) indium (In) $3d_{5/2}$ and b) tin (Sn) $3d_{5/2}$ collected from OAm-ITO NPs. The deconvoluted peaks in the In $3d_{5/2}$ core-level spectrum (a) could be divided into three doublets that corresponded to three different oxidation states of the In atoms. More specifically, the main peak was deconvoluted into: (1) an In^{0-2+}peak (443.0 eV) caused by the presence of oxygen vacancy states; (2) an In^{3+}peak (444.2 eV) caused by the fully oxidized state, such as In_2O_3; and (3) an $In(OH)_x$ peak (445.4 eV) caused by the In atoms with surface oxygen atoms or hydroxyl groups.[S1,S2] The ratios of the In^{0-2+}, In^{3+}, and $In(OH)_x$ states among the In atoms in the OAm-ITO NPs were estimated to be approximately 6.6%, 52.2%, and 41.2%, respectively. The Sn $3d_{5/2}$ spectrum (b) was deconvoluted into Sn^{0-2+} $3d_{5/2}$ (485.0 eV), Sn^{2+} $3d_{5/2}$ (485.9 eV), and Sn^{4+} $3d_{5/2}$ (486.6 eV) peaks.[S2,S3] The ratio of the Sn^{4+} oxidation state was also estimated to be approximately 70.3%.

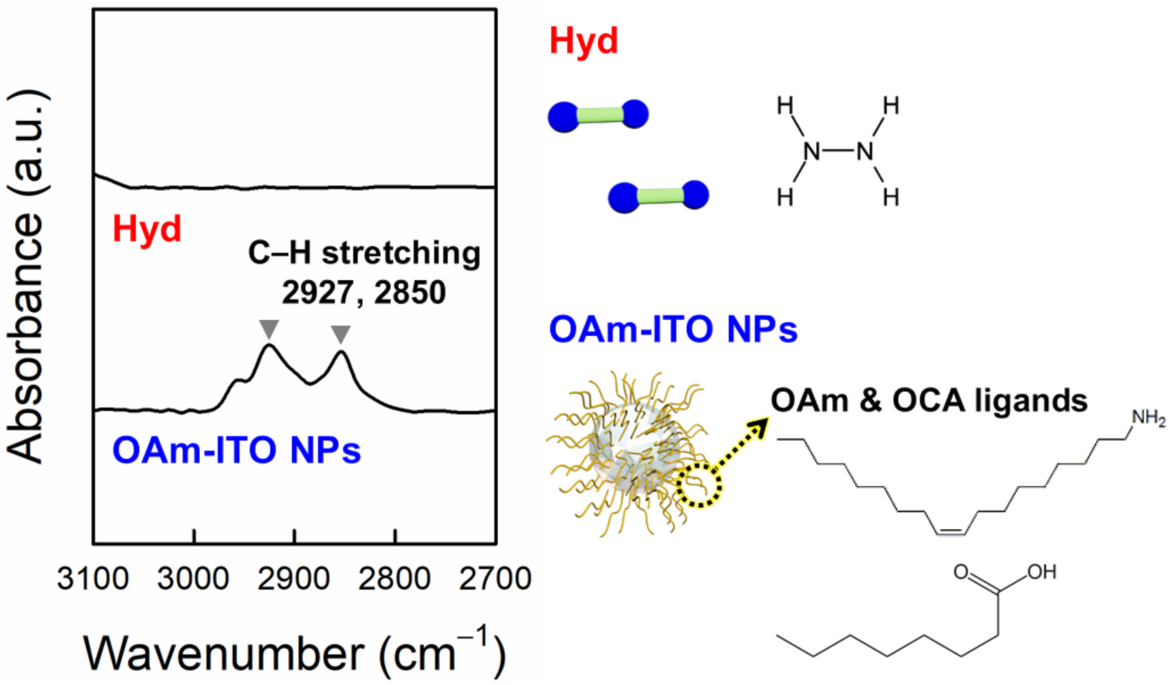

Figure S4. FTIR spectra of pristine OAm and OCA-stabilized ITO NPs (i.e., OAm-ITO NPs) and Hyd. In the case of the OAm-ITO NPs, the C–H stretching peaks (~2,927 and ~2,850 cm^{-1}) derived from the long alkyl chains of the OAm and OCA ligands were shown. However, in the case of the Hyd, no distinct peak appeared in that range.[S4]

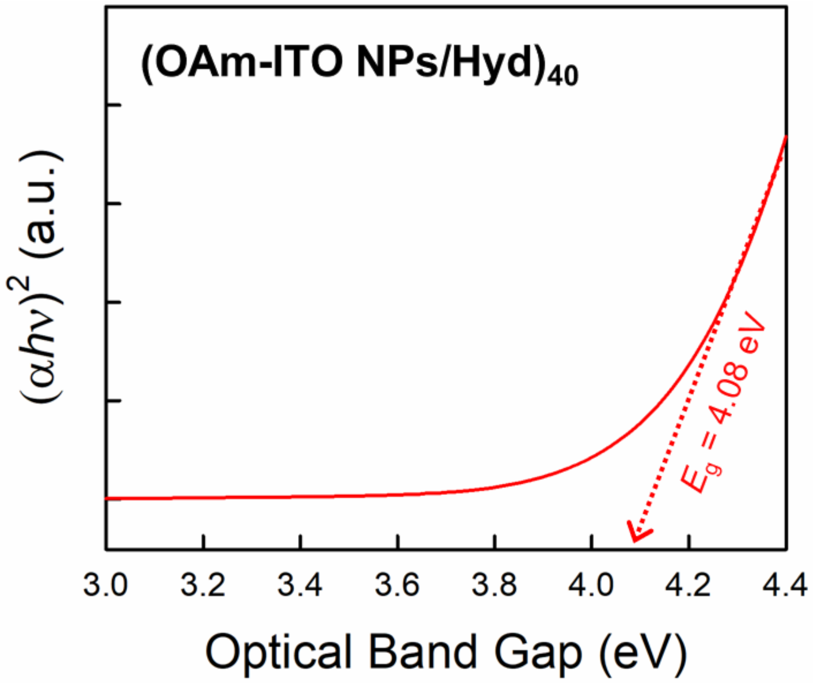

Figure S5. The optical band gap of (OAm-ITO NPs/Hyd)$_{40}$ multilayers, obtained using the Tauc plot from UV–visible spectra.[S5]

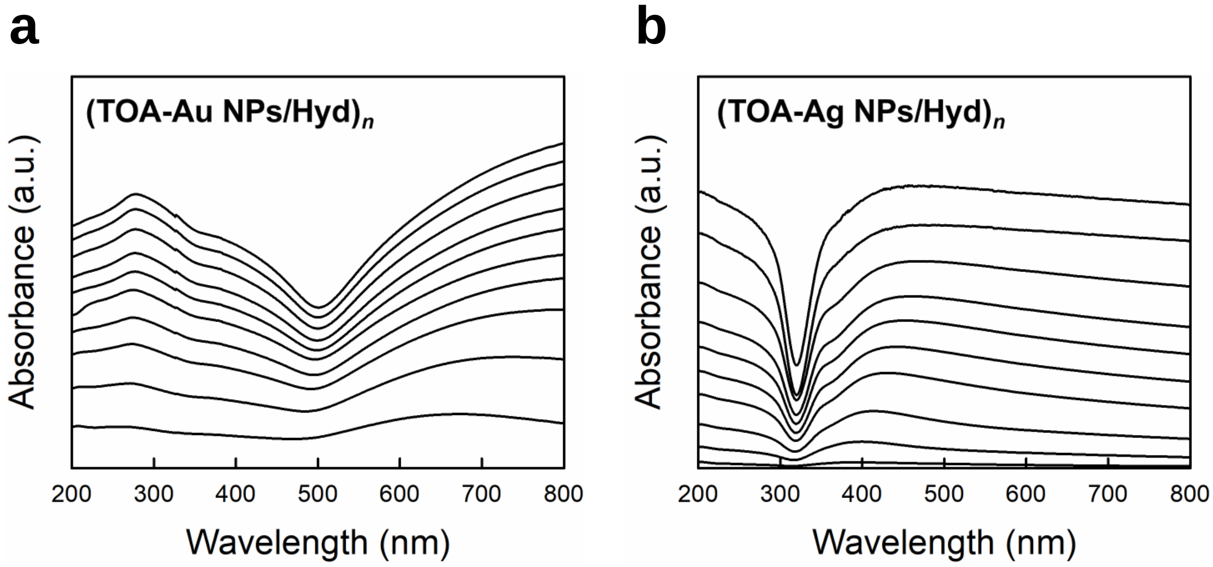

Figure S6. UV–visible absorbance spectra of a) (TOA-Au NP/Hyd)$_n$ and b) (TOA-Ag NP/Hyd)$_n$ multilayers with increasing bilayer number (n).

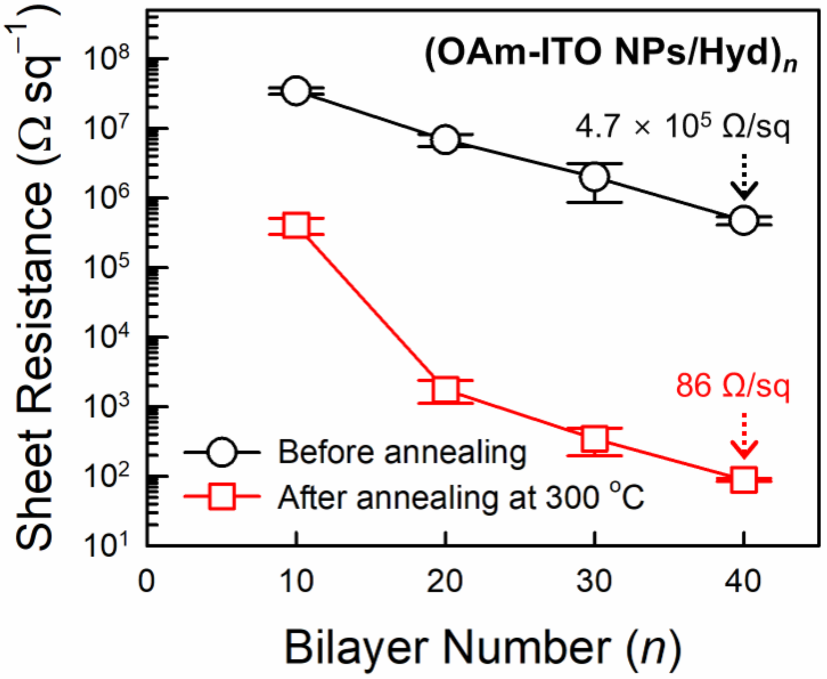

Figure S7. Sheet resistance of (OAm-ITO NPs/Hyd)$_n$ multilayers on glass substrates before (black circles) and after (red squares) thermal annealing at 300 □ as a function of bilayer number (*n*).

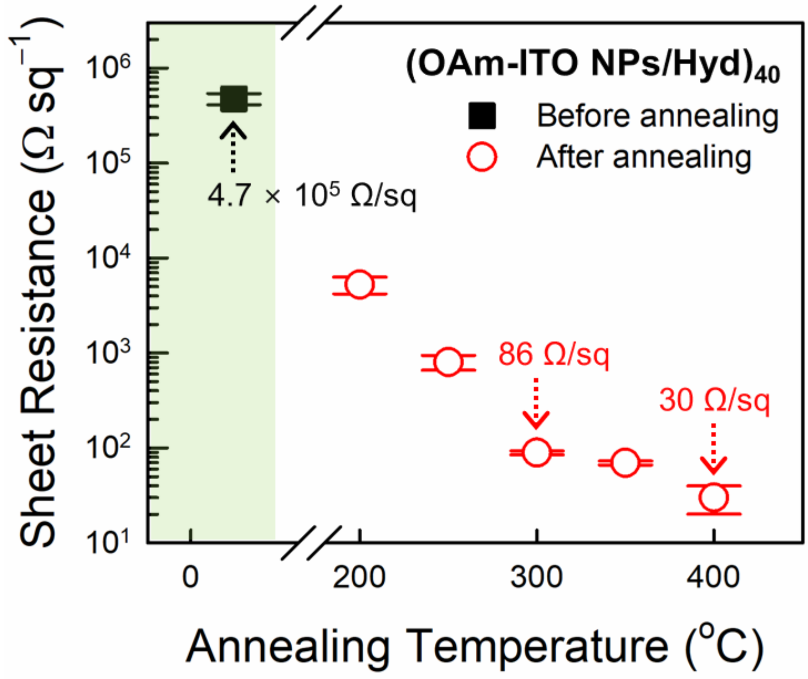

Figure S8. Sheet resistance of (OAm-ITO NPs/Hyd)$_{40}$ multilayers on glass substrates before and after thermal annealing with increasing annealing temperature from 200 to 400 □.

Table S2. Comparison of optical/electrical performance of ITO NP-based TCO electrodes.

Materials	Method	Thickness (nm)	Transmittance at 550 nm (%)	Sheet resistance (Ω sq^{-1})	Annealing condition	Reference
ITO NPs	**LbL assembly**	**299**	**89.6**	**86**	**300 ℃, 3 h (under H_2/Ar)**	**Our work**
ITO NPs	**LbL assembly**	**299**	**87.0**	**30**	**400 ℃, 3 h (under H_2/Ar)**	**Our work**
ITO NPs	Spin-coating	146	87.0*	358	300 ℃, 6 h (under H_2/Ar)	[S6]
ITO NPs	Spin-coating	146	-	118	400 ℃, 6 h (under H_2/Ar)	[S6]
ITO NPs	Spin-coating	300	83.0*	110	300 ℃, 6 h (under H_2/Ar)	[S7]
ITO NPs	Spin-coating	195	88.0	133	120 ℃, 10 min + 300 ℃, 1h (under H_2/Ar)	[S8]
ITO NPs	Spin-coating	191	90.0	466	300 ℃, 2 h (under H_2/Ar)	[S9]
ITO NPs	Spin-coating	200	88.0*	1316*	420 ℃, 40 min (under air)	[S10]
ITO NPs	Ink-jet printing	750	88.1	203	450 ℃, 4 min (under N_2/O_2)	[S11]

* Optical and/or electrical performance was evaluated from the given data in the literature.

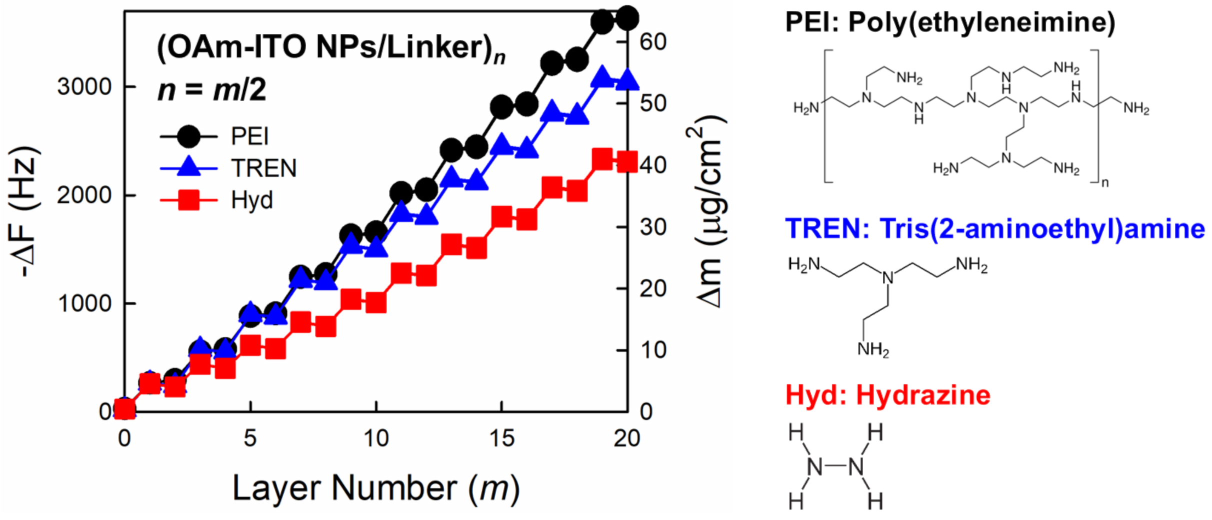

Figure S9. Frequency and mass changes of (OAm-ITO NPs/Linker)$_n$ multilayers obtained from QCM measurements for PEI (black circle), TREN (blue triangles) and Hyd (red squares) linkers and the molecular structure of linkers. The average loading amount of (OAm-ITO NPs/PEI), (OAm-ITO NPs/TREN), and (OAm-ITO NPs/Hyd) bilayers resulted in a Δm of ~6.40, ~5.36, ~4.0 μg cm^{-2}, respectively.

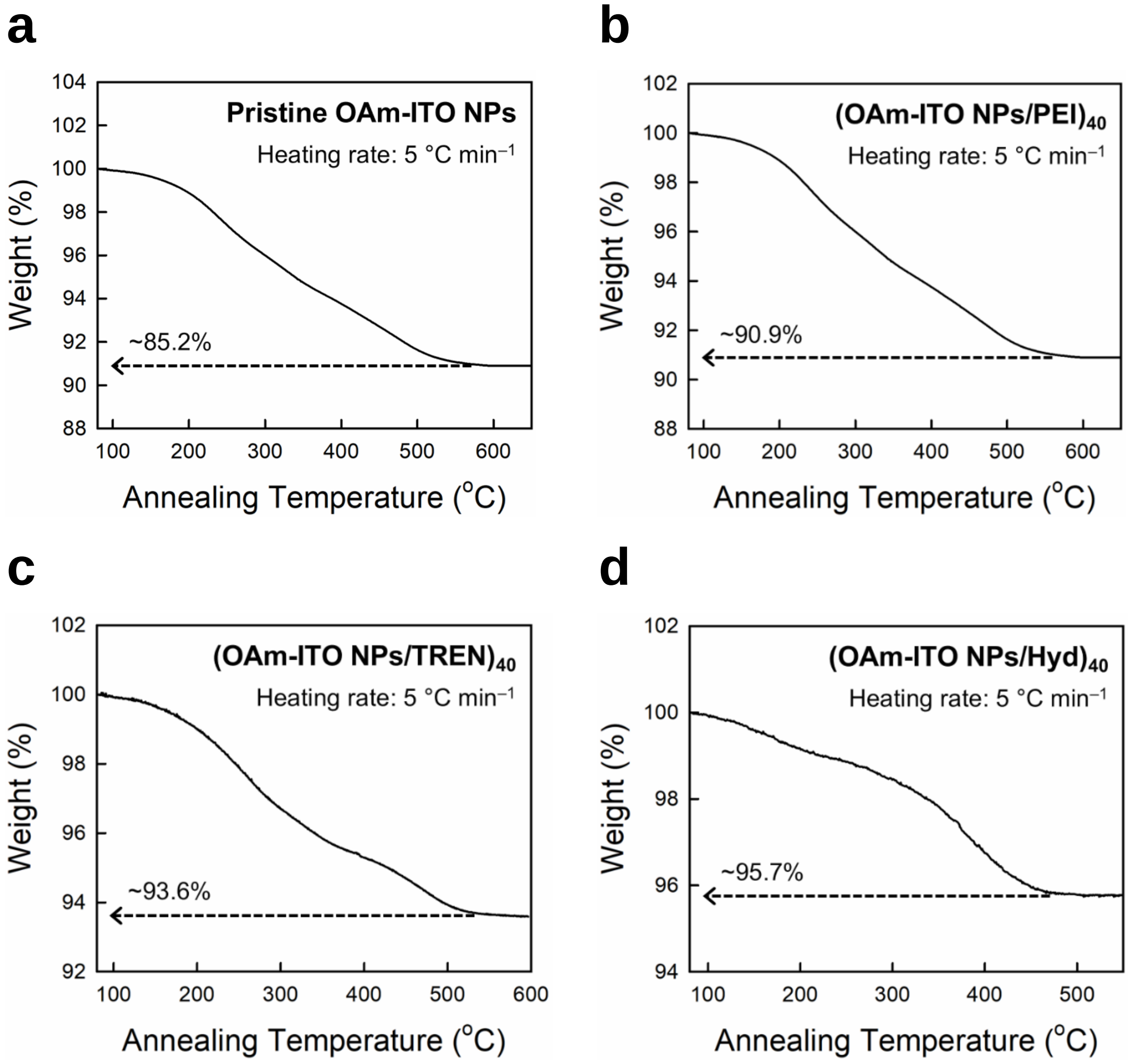

Figure S10. TGA profiles of a) pristine OAm-ITO NPs, b) (OAm-ITO NPs/PEI)$_{40}$, c) (OAm-ITO NPs/TREN)$_{40}$, and d) (OAm-ITO NPs/Hyd)$_{40}$ multilayers. In this case, the organic composition of pristine OAm-ITO NPs was relatively higher than those of amine-functionalized linker-based multilayers due to the presence of their bulky native ligands. The compositions of ITO NPs within the multilayers were estimated to be ~90.9 (PEI), ~93.6 (TREN), and ~95.7% (Hyd), respectively. Resultantly, taking into account the QCM measurements (**Figure S9, Supporting Information**), the loading amount of ITO NPs within the PEI, TREN, and Hyd linker-based multilayers was calculated to be approximately 5.82, 5.02, and 3.83 µg cm^{-2}, respectively.

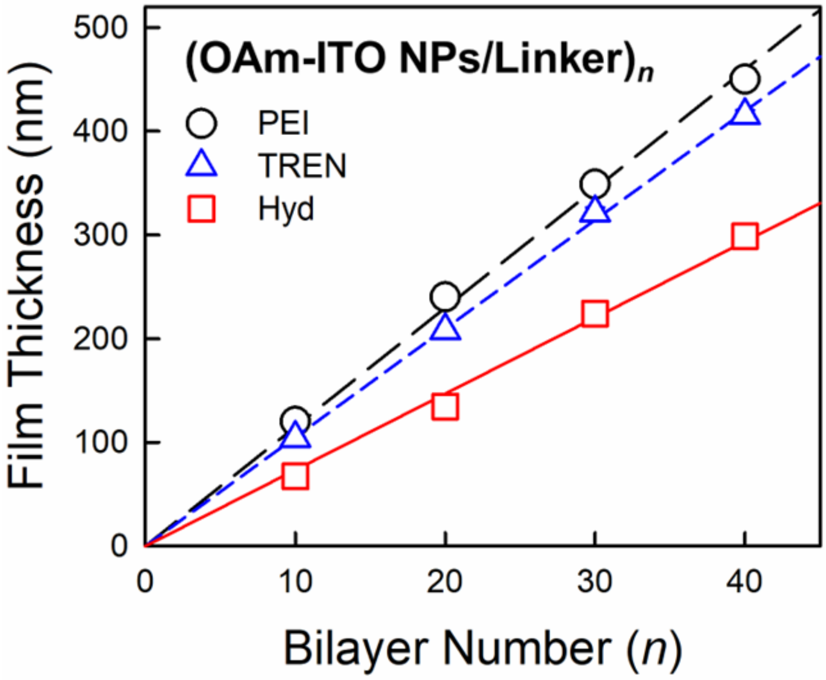

Figure S11. Total thickness change of (OAm-ITO NPs/Linker)$_n$ multilayers on Si wafers for PEI (black circle), TREN (blue triangles), and Hyd (red squares) linkers.

Table S3. Electrical and optical properties of (OAm-ITO NPs/Linker)$_n$ multilayers treated under the same annealing conditions (temperature: 300 □; time: 3 hours; atmosphere: 95% Ar gas and 5% H_2 gas).

Film notation	Thickness (nm)	Transmittance at 550 nm (%)	Sheet resistance (Ω sq^{-1})	Electrical conductivity (S cm^{-1})	Resistivity (Ω cm)	Hall carrier concentration (10^{20} cm^{-3})	Hall mobility (cm^2 V^{-1} s^{-1})
(OAm-ITO NPs/Hyd)$_{10}$	70	89.7	4.1×10^5	0.348	2.87	1.92	0.27
(OAm-ITO NPs/Hyd)$_{20}$	146	88.3	1.8×10^3	38.1	2.6×10^{-2}	2.56	1.23
(OAm-ITO NPs/Hyd)$_{30}$	224	90.8	345	129	7.8×10^{-3}	3.42	2.87
(OAm-ITO NPs/Hyd)$_{40}$	299	89.6	86	389	2.6×10^{-3}	5.82	8.35
(OAm-ITO NPs/PEI)$_{40}$	447	70.5	2.3×10^5	9.7×10^{-2}	10.3	0.4	0.14
(OAm-ITO NPs/TREN)$_{40}$	410	86.9	346	70.5	1.4×10^{-2}	4.63	1.42

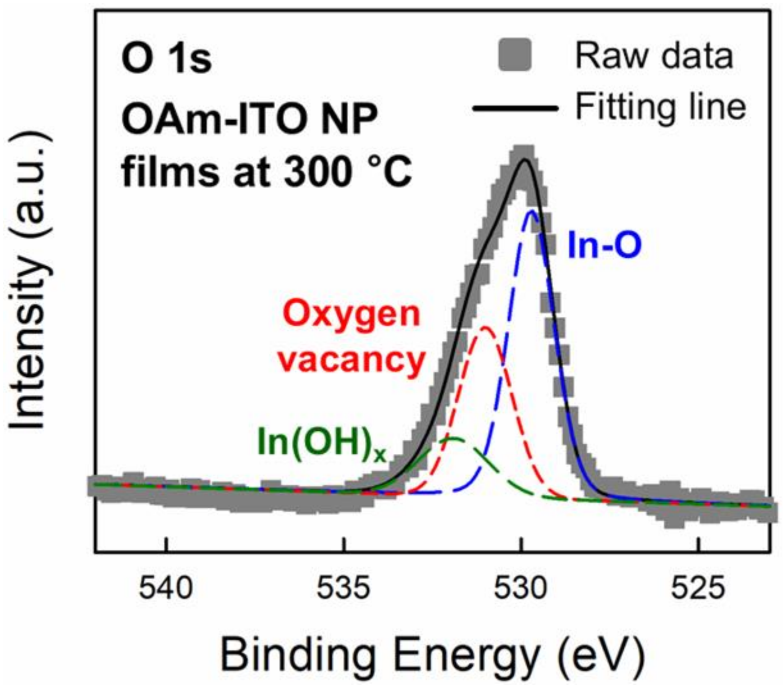

Figure S12. Deconvoluted XPS spectra of O 1s peaks collected from solution-cast OAm-ITO NP films after thermal annealing at 300 °C. The oxygen vacancy states in thermally annealed OAm-ITO NP films were estimated to be ~33.0%.

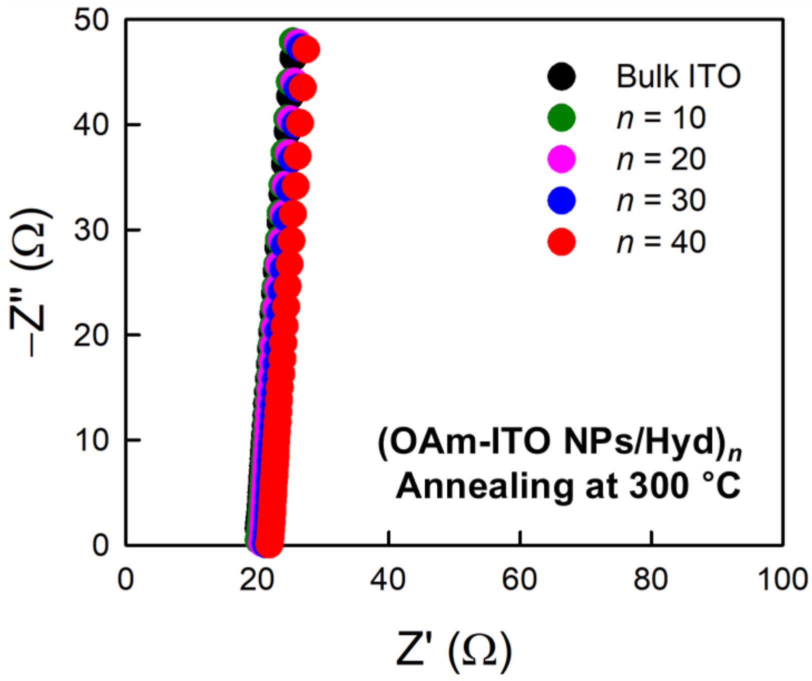

Figure S13. Nyquist plots of (OAm-ITO NPs/Hyd)$_n$ multilayers after thermal annealing at 300 °C with increasing bilayer number (*n*) from 10 to 40.

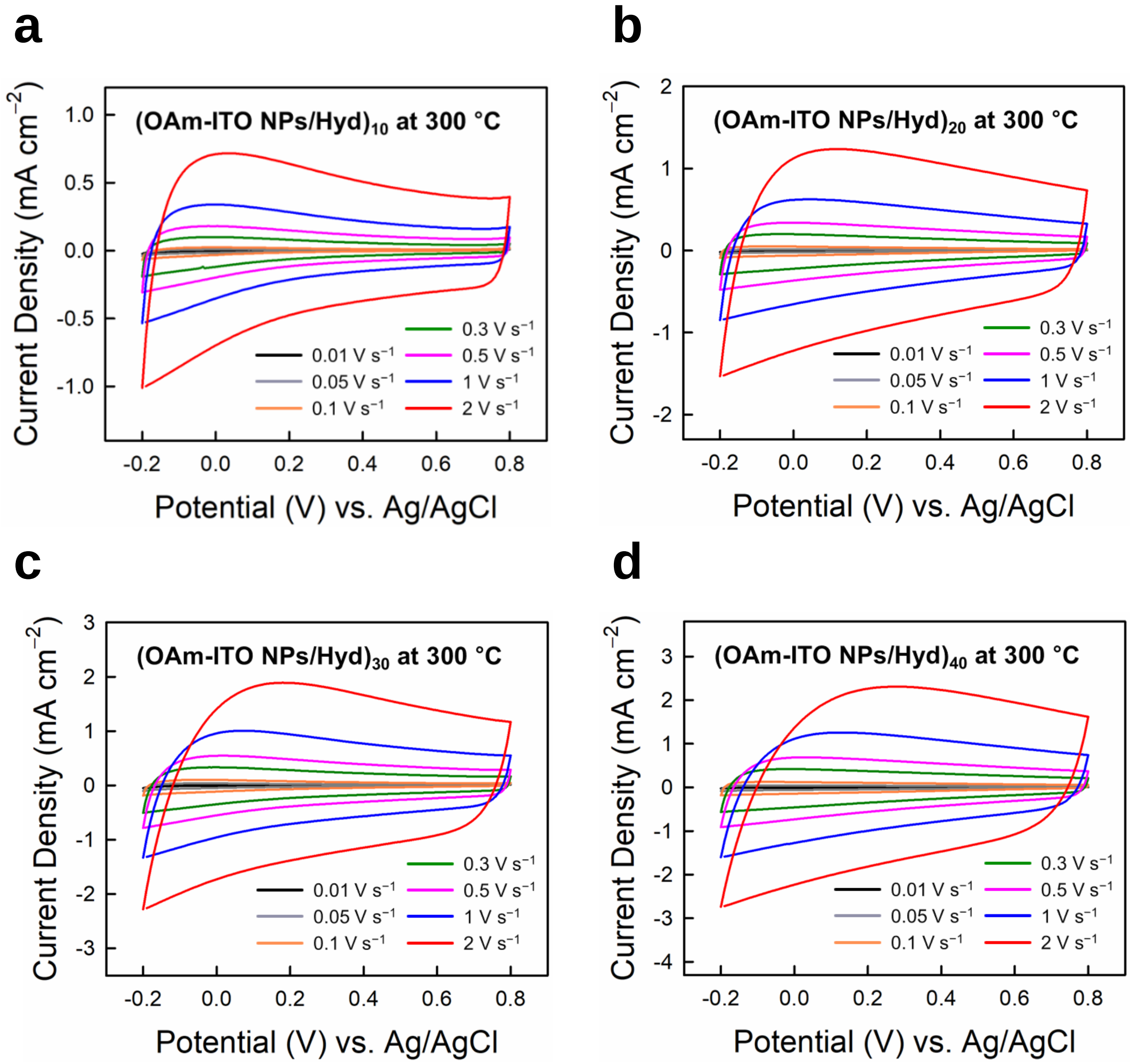

Figure S14. CV curves of (OAm-ITO NPs/Hyd)$_n$ multilayers after thermal annealing at 300 °C with increasing scan rates from 0.01 to 2 V s^{-1} for different bilayer numbers: a) n = 10, b) n = 20, c) n = 30, and d) n = 40.

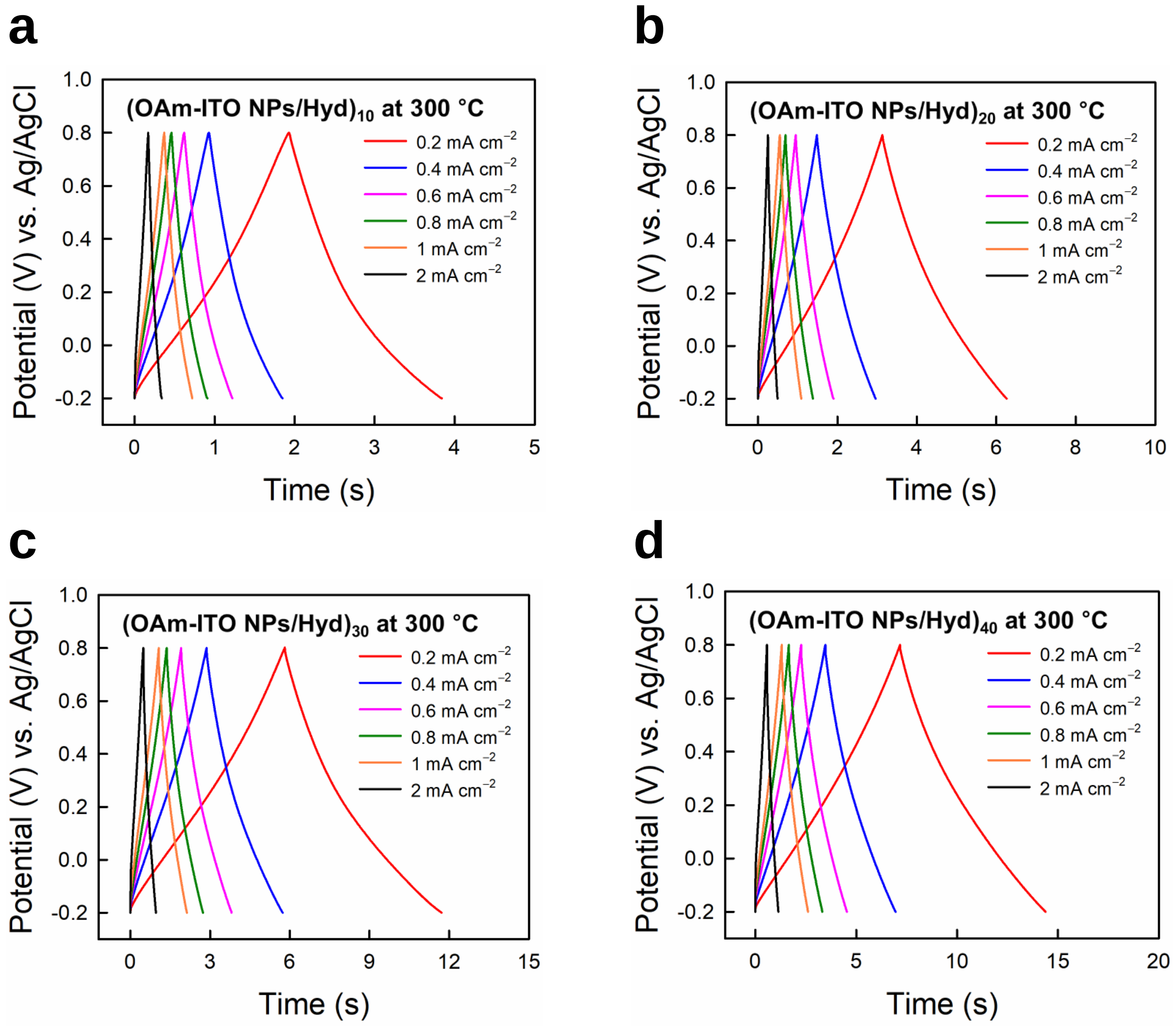

Figure S15. GCD profiles of (OAm-ITO NPs/Hyd)$_n$ multilayers after thermal annealing at 300 °C with increasing current densities from 0.2 to 2 mA cm^{-2} for different bilayer numbers: a) n = 10, b) n = 20, c) n = 30, and d) n = 40.

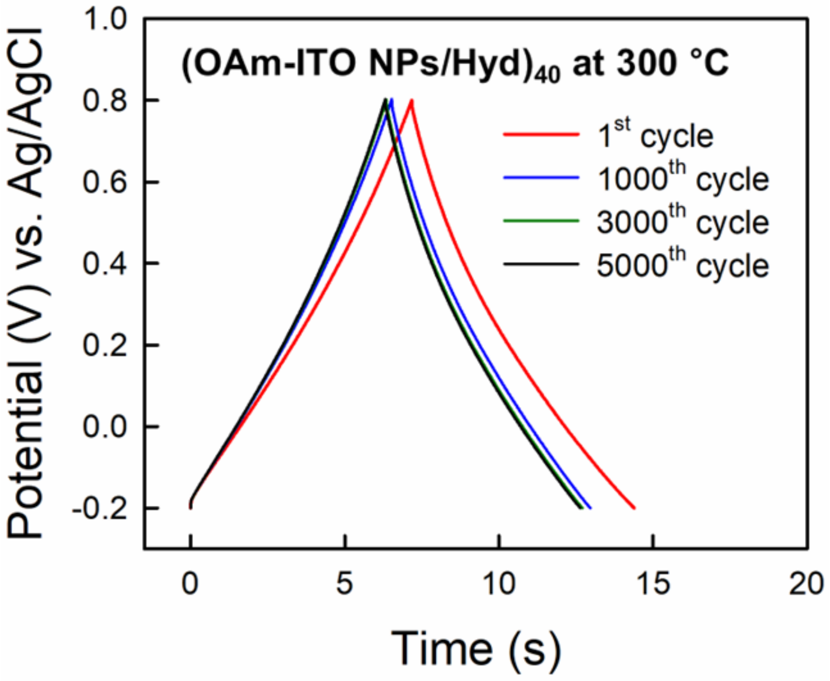

Figure S16. GCD profiles of (OAm-ITO NPs/Hyd)$_{40}$ multilayers for 1st, 1000th, 3000th, and 5000th cycles in the cycling tests.

Video S1. Video showing (OAm-ITO NPs/Hyd)$_{40}$ multilayers on a high-curvature bulb glass connected with an LED after thermal annealing at 300 □.

Supplementary References

[S1] S. Y. Lee, J. Kim, A. Park, J. Park, H. Seo, *ACS Nano* **2017**, *11*, 6040.

[S2] A. Thogersen, M. Rein, E. Monakhov, J. Mayandi, S. Diplas, *J. Appl. Phys.* **2011**, *109*, 113532.

[S3] M. Kwok, L. Ottaviano, M. Passacantando, S. Santucci, G. Czempik, J. Szuber, *Thin*

Solid Films **2005**, *490*, 36.

[S4] M. Brahmayya, Shenghong A. Dai, S.-Y. Suen, *RSC Adv.* **2015**, *5*, 65351.

[S5] C. Kim, Y.-H. Kim, Y.-Y. Noh, S.-J. Hong, M. J. Lee, *Adv. Electron. Mater.* **2018**, *4*, 1700440.

[S6] J. Lee, S. Lee, G. Li, M. A. Petruska, D. C. Paine, S. Sun, *J. Am. Chem. Soc.* **2012**, *134*, 13410.

[S7] J. Song, S. A. Kulinich, J. Li, Y. Liu, H. Zeng, *Angew. Chem. Int. Ed.* **2015**, *127*, 472.

[S8] J. Lee, M. A. Petruska, S. Sun, *J. Phys. Chem. C* **2014**, *118*, 12017.

[S9] Z. Chen, X. Qin, T. Zhou, X. Wu, S. Shao, M. Xie, Z. Cui, *J. Mater. Chem. C* **2015**, *3*, 11464.

[S10] M. Yarema, S. Pichler, D. Kriegner, J. Stangl, O. Yarema, R. Kirchschlager, S. Tollabimazraehno, M. Humer, D. Häringer, M. Kohl, G. Chen, W. Heiss, *ACS Nano* **2012**, *6*, 4113.

[S11] J.-A. Jeong, J. Lee, H. Kim, H.-K. Kim, S.-I. Na, *Sol. Energy Mater. Sol. Cells* **2010**, *94*, 1840.